AIAA JOURNAL
Vol. 45, No. 8, August 2007

Direct Numerical Simulations of Flow Past an Array of Distributed Roughness Elements

Donald P. Rizzetta* and Miguel R. Visbal†
U.S. Air Force Research Laboratory, Wright–Patterson Air Force Base, Ohio 45433-7512

DOI: 10.2514/1.25916

Direct numerical simulation was used to describe the subsonic flow past an array of distributed cylindrical roughness elements mounted on a flat plate. Solutions were obtained for element heights corresponding to a roughness-based Reynolds number (Re_k) of both 202 and 334. The numerical method used a sixth-order-accurate centered compact finite difference scheme to represent spatial derivatives, which was used in conjunction with a tenth-order low-pass Pade-type nondispersive filter operator to maintain stability. An implicit approximately factored time-marching algorithm was employed, and Newton-like subiterations were applied to achieve second-order temporal accuracy. Calculations were carried out on a massively parallel computing platform, using domain decomposition to distribute subzones on individual processors. A high-order overset grid approach preserved spatial accuracy on the mesh system used to represent the roughness elements. Features of the flowfields are described, and results of the computations are compared with experimentally measured velocity components of the time-mean flowfield, which are available only for $Re_k = 202$. Flow about the elements is characterized by a system of two weak corotating horseshoe vortices. For $Re_k = 334$, an unstable shear layer emanating from the top of the cylindrical element generated nonlinear unsteady disturbances of sufficient amplitude to produce explosive bypass transition downstream of the array. The $Re_k = 202$ case displayed exponential growth of turbulence energy in the streamwise direction, which may eventually result in transition.

Nomenclature

D	=	roughness element diameter, 6.35 mm
E_f, E_{k_z}	=	frequency and spanwise wave number of $(u - \bar{u})^2$
E_i	=	planar integrated fluctuation energy
f	=	frequency, Hz
h	=	roughness element height, mm
I, J, K	=	coordinate grid indices in the streamwise, vertical, and spanwise directions
k_z	=	nondimensional spanwise wave number
l	=	reference length used for nondimensionalization, 1 mm
Re	=	reference Reynolds number, $\rho_\infty u_\infty l/\mu_\infty$
Re_k	=	roughness-based Reynolds number, $\rho_\infty u_B(h)h/\mu_\infty$
Re_{δ^*}	=	displacement thickness-based Reynolds number, $\rho_\infty u_\infty \delta^*/\mu_\infty$
u, v, w	=	nondimensional Cartesian velocity components in the x, y, z directions
$u_B(h)$	=	value of the Blasius streamwise velocity component evaluated at h
x, y, z	=	nondimensional Cartesian coordinates in the streamwise, vertical, and spanwise directions
x_l	=	streamwise location of roughness elements
x_{vle}	=	streamwise location of the plate virtual leading edge
δ	=	nondimensional theoretical flat-plate boundary-layer thickness, $[(x - x_{\text{vle}})/Re]^{1/2}$
δ^*	=	dimensional theoretical flat-plate boundary-layer displacement thickness
η_b	=	nondimensional boundary-layer coordinate, y/δ
λ	=	nondimensional roughness element spanwise spacing
ω_x, ω_z	=	streamwise and spanwise components of vorticity

Subscripts

e	=	evaluated at boundary-layer edge

Superscripts

$-$	=	time-mean quantity
$'$	=	root-mean-square fluctuating component
$+$	=	law-of-the-wall coordinate

I. Introduction

THE transition from laminar to turbulent flow in a flat-plate boundary layer is one of the most fundamental and often studied subjects in fluid mechanics. Although this canonical problem is basic in nature, it can provide a framework for understanding more complex and practical situations encountered in modern aerospace vehicles. One specific aspect of this topic is the role played by roughness elements in the transition process. When the height of a roughness element is sufficiently small, the disturbance field that it generates may consist of very weak fluctuations, and is often considered to be stationary. The perturbation to a Blasius boundary layer can result in structures spatially evolving behind the element, which have an initial region of algebraic growth in the kinetic energy, followed by exponential decay further downstream. This phenomenon is commonly referred to as transient growth, and has several interesting properties. Although transient growth can amplify certain types of disturbances in the subcritical region of boundary layers, it is also capable of suppressing the growth of Tollmien–Schlichting waves, thereby delaying the transition to turbulence [1]. For more sizable roughness elements, large-amplitude disturbances are produced, leading to a breakdown of the evolving structures and bypass transition in the region subcritical to Tollmien–Schlichting wave growth.

A detailed chronological description of attempts to explain both the physical and mathematical nature of transient growth, may be found in [2]. This includes a number of investigations which are based upon various forms of stability analyses.

A number of experimental studies have described behavior that is consistent with that of transient growth, including examinations of

Presented as Paper 3527 at the 36th AIAA Fluid Dynamics Conference, San Francisco, CA, 5–8 June 2006; received 15 June 2006; revision received 10 April 2007; accepted for publication 13 April 2007.

*Senior Research Aerospace Engineer, Computational Sciences Branch, AFRL/VAAC. Associate Fellow AIAA.

†Technical Area Leader, Computational Sciences Branch, U.S. Air Force Research Laboratory/VAAC. Associate Fellow AIAA.

distributed surface roughness [3,4] and those of freestream turbulence [5–9]. Among these, only the work of Breuer and Haritonidis [5] was performed to compare with transient growth theories. More recently, a series of experiments [1,2,10–13] for distributed roughness elements has been conducted to verify several aspects of the characteristics predicted by transient growth analyses. In addition, the data collected from these experiments is useful for corroboration of numerical simulation. This body of work considers not only the transient growth produced by roughness elements of small height, but also Tollmien–Schlichting wave suppression and the initiation of bypass transition for the case of larger elements.

There are few direct numerical simulations which have attempted to reproduce the flow about roughness elements. The computations of Joslin and Grosch [14] examined growth characteristics downstream of a "shallow" bump, where the configuration and flow conditions corresponded to the experiment of Gaster et al. [15]. Although results of the simulations were consistent with experimental observations, no quantitative comparisons were made. The works of Fischer and Choudhari [16,17] carried out computations for distributed roughness elements that were considered experimentally by White et al. [2,10–12]. Some aspects of the simulations compared favorably with the experiments for roughness heights which produced only transient growth. Modal amplitudes of the streamwise kinetic energy for these cases, however, were considerably lower than measurements. Moreover, for a larger roughness height which resulted in bypass transition in the experiment, transition did not occur in the simulation. It was suggested by Choudhari and Fischer [17] that the reason transition did not occur in this situation may have been due to a lack of sufficient spatial resolution, and/or that the extent of the computational domain downstream of the roughness element was inadequate.

Although the studies of White et al. [2,10–12] sought to investigate the transient growth phenomenon, due to the sensitive nature of the physical situation, practical limitations of wind-tunnel experiments may have introduced growing disturbances into the flow. These limitations include small but finite freestream turbulence levels, and operating conditions (based upon Re_{δ^*}) that may lie in the unstable regime. Some of these aspects might be clarified by companion direct numerical simulations, which can also serve to qualify the measurements. It is the purpose of the present work to provide computations which correspond to the experiments of [2,10–12] for the flow over a distributed array of roughness elements. Cases which exhibited both transient growth and bypass transition in the experiments are considered. Details of the simulations are described, characteristics of the solutions are elucidated, and quantitative comparisons of the computed results are made with the available experimental data in terms of time-mean velocity components of the flowfield.

II. Governing Equations and Numerical Method

The governing equations are taken as the unsteady three-dimensional compressible unfiltered Navier–Stokes equations. After introducing a curvilinear coordinate transformation to a body-fitted system, the equations are cast in the following nondimensional conservative form

$$\frac{\partial}{\partial t}\left(\frac{\boldsymbol{Q}}{\mathcal{J}}\right)+\frac{\partial}{\partial \xi}\left(\boldsymbol{F}-\frac{1}{Re}\boldsymbol{F}_v\right)+\frac{\partial}{\partial \eta}\left(\boldsymbol{G}-\frac{1}{Re}\boldsymbol{G}\right)+\frac{\partial}{\partial \zeta}\left(\boldsymbol{H}-\frac{1}{Re}\boldsymbol{H}_v\right)=0 \tag{1}$$

Here t is the time, ξ, η, ζ the computational coordinates, $\boldsymbol{Q}$ the vector of dependent variables, $\boldsymbol{F}, \boldsymbol{G}, \boldsymbol{H}$ the inviscid flux vectors, and $\boldsymbol{F}_v, \boldsymbol{G}_v, \boldsymbol{H}_v$ the viscous flux vectors.

Time-accurate solutions to Eq. (1) are obtained numerically by the implicit approximately factored finite difference algorithm of Beam and Warming [18] employing Newton-like subiterations [19], which has evolved as an efficient tool for generating solutions to a wide variety of complex fluid flow problems. Second-order-accurate, backward-implicit time differencing was used to obtain temporal derivatives.

The implicit segment of the algorithm incorporates second-order-accurate centered differencing for all spatial derivatives, and uses nonlinear artificial dissipation [20] to augment stability. Efficiency is enhanced by solving this implicit portion of the factorized equations in diagonalized form [21]. Temporal accuracy, which can be degraded by use of the diagonal form, is maintained by using subiterations within a time step. This technique has been commonly invoked to reduce errors due to factorization, linearization, diagonalization, and explicit application of boundary conditions. It is useful for achieving temporal accuracy on overset zonal mesh systems, and for a domain decomposition implementation on parallel computing platforms. Any deterioration of the solution caused by use of artificial dissipation and by lower-order spatial resolution of implicit operators is also reduced by the procedure. Three subiterations per time step have been applied to preserve second-order temporal accuracy in the present application.

The compact difference scheme which is employed to evaluate spatial derivatives for the explicit part of the factored form of Eq. (1) is based upon the pentadiagonal system of Lele [22], and is capable of attaining spectral-like resolution. This is achieved through the use of a centered implicit difference operator with a compact stencil, thereby reducing the associated discretization error. For the present computations, a sixth-order tridiagonal subset of Lele's system is used. The scheme has been adapted by Visbal and Gaitonde [23] as an implicit iterative time-marching technique, applicable for unsteady vortical flows. It is used in conjunction with a tenth-order low-pass Pade-type nondispersive spatial filter developed by Gaitonde et al. [24], which has been shown to be superior to the use of explicitly added artificial dissipation for maintaining both stability and accuracy on stretched curvilinear meshes [23]. The filter is applied to the solution vector sequentially in each of the three computational directions following each subiteration. A more thorough description of the governing equations and complete details of the numerical method appear in [25], but have been omitted here for brevity. Application of the subiteration process and use of the high-order filter scheme, results in solutions with sixth-order spatial and second-order temporal accuracy.

The aforementioned features of the numerical algorithm are embodied in a parallel version of the time-accurate, three-dimensional computer code FDL3DI [26], which has proven to be reliable for steady and unsteady fluid flow problems, including the simulation of flows over delta wings with leading-edge vortices [27–29], vortex breakdown [28,29], direct numerical simulation of transitional wall jets [30] and synthetic jet actuators [31], and direct numerical and large-eddy simulation of subsonic [32–35] and supersonic flowfields [36–38].

III. Details of the Computations

Experimental measurements for the roughness array were obtained in the boundary layer of a flat aluminum plate that was polished to a near mirror finish, and is illustrated schematically in Fig. 1. The plate had an elliptical leading edge and a trailing-edge flap which was used to control the stagnation streamline. A spanwise array of cylindrical roughness elements was located a distance $x_l = 300$ mm downstream from the physical leading edge of the plate. Through the use of a nonlinear least-squares curve fit to the boundary-layer displacement and momentum thicknesses as a

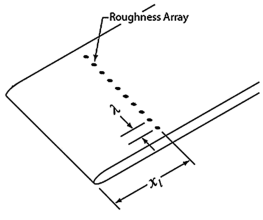

Fig. 1 Schematic illustration of experimental configuration.

function of streamwise position, it was estimated that a virtual leading edge of the configuration was located 7 mm upstream of the physical leading edge.

The roughness elements were constructed from circular adhesive-backed paper labels that could be stacked vertically to provide a range of desired roughness heights. These labels were 6.350 mm in diameter and 1.016×10^{-4} m thick. Seven and nine layers were used to obtain element heights of 0.710 and 0.915 mm, corresponding to roughness-based Reynolds numbers Re_k of 202 and 334, respectively. From a large body of experimental investigations, it was found that for isolated three-dimensional roughness elements, the critical value of Re_k at which transition should occur is given by $600(h/D)^{0.4}$ [39]. These critical values are 250 for $Re_k = 202$ and 276 for $Re_k = 334$, indicating transition for the taller element only.

The freestream velocity of 12.2 m/s resulted in a reference Reynolds number of $Re = 769.0$ and Mach number of 0.055. For numerical simulations, a value of $M_\infty = 0.1$ was specified. Spanwise spacing of the elements was set at approximately three times the elemental diameter such that $\lambda = 19.0$. This distance was sufficient to ensure that each protuberance acted as an isolated element in the near-wake region [40]. The entire experimental arrangement consisted of 12 elements to establish predominantly periodic flow in the central region of the array where measurements were performed. Thus, for the numerical computations, only a single roughness element was simulated, and periodic conditions were invoked in the spanwise direction.

A. Computational Mesh System

An overset mesh system with its origin located at the center of the roughness element was composed of three distinct topological regions which are seen in Fig. 2, where for clarity only a fraction of the total grid points are shown. A primary zone comprising the majority of the flat-plate region used a nonuniform Cartesian construct of $(713 \times 201 \times 155)$ grid points in (I, J, K). The usable domain size for this region was defined by

$$-63.5 \le x \le 212.5, \qquad 0.0 \le y \le 5.0, \qquad -9.5 \le z \le 9.5 \tag{2}$$

which does not include the coarse-mesh areas near the upper and downstream boundaries, which extended to $x = 312.5$ and $y = 110.0$. Within the usable region, there were 698 points in the I direction and 150 in the J direction. For the upstream and downstream portion of the flowfield, $\Delta x = 0.5$, and near to the roughness element $\Delta x = 0.125$. At the plate surface for $Re_k = 334$, the minimum vertical spacing was $\Delta y = 0.0183$, so that 51 J grid points were used to define the roughness element. The nonuniform vertical distribution provided 130 points in the boundary-layer profile at the inflow plane. A uniform mesh spacing was employed in the spanwise direction with $\Delta z = 0.127$.

Within the primary zone, a portion of the grid points forming the section

$$-5.25 \le x \le 5.25, \qquad 0.00 \le y \le 3.18, \qquad -5.32 \le z \le 5.32 \tag{3}$$

were removed and replaced with a cylindrical topology used to describe the roughness element. This zone was formed by $(141 \times 361 \times 145)$ mesh points in the radial, circumferential, and vertical directions, respectively, and can be observed in Fig. 2. The minimum radial grid spacing in this region was 0.0183, and the circumferential spacing was uniform. Grid points lying interior to the element geometric boundary were removed. The O-grid construct about the cylindrical element maintained a minimum radial distance greater than zero from the origin to preclude the emergence of a polar axis. This resulted in a circular hole along the y axis for the cylindrical zone above the top of the roughness element. An auxiliary $(61 \times 95 \times 61)$ Cartesian mesh was used to fill the hole, and to connect the top of the cylinder with the primary zone. The total number of grid points in the complete mesh system was approximately 28.8×10^6. For overset regions connecting the respective zones, a minimum five-grid point overlap was enforced in each coordinate direction to preserve the high-order differencing and filtering schemes. In addition to the grid system just described, a coarse-mesh arrangement was also generated by removing every other point in each coordinate direction from all zones.

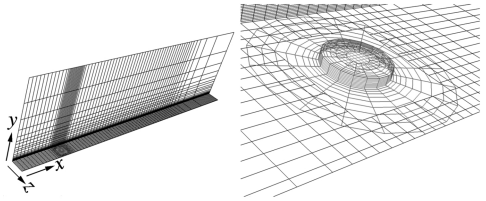

Fig. 2 Computational mesh system.

B. Domain Decomposition

For parallel processing, the computational mesh system was decomposed into a series of subzones, which were then distributed on individual processors of a massively parallel computing platform (IBM SP4+). Decompositions were constructed to provide an approximately equal number of grid points in every subzone, thereby balancing the computational work load among the processors. Faces at the boundaries of each subzone block were overset into adjacent domains, such that an overlap of five planes was established. Although this incurred an overhead due to redundant computation, it maintained the formal high-order accuracy of both the numerical differencing and filtering schemes. A vast majority of the grid points in the overlapping regions of respective subzones were coincident with those of neighboring subzones. In these situations, no interpolation was required for the transfer of information between the subzones. Flow variables in regions of noncoincident overlapped meshes, however, were obtained from explicit sixth-order accurate Lagrangian interpolation formulas. This interpolation approach for high-order numerical solutions has been successfully applied by Sherer [41] and Sherer and Scott [42] for the computation of fluid dynamic and acoustic problems, and by Rizzetta and Visbal [34,35] for direct simulation of transitional turbine blade flowfields. Automated software [43] was used to identify donor and recipient grid points in the overlapping domains. Internode communication among the processors was established through standard message-passing interface (MPI) library routines [44], which were used to transfer information between the various subzones of the flowfield at domain boundaries. A total of 391 processors were employed for the computations reported here, apart from those performed on the coarse-mesh system which used 54.

C. Inflow Profiles

Inflow profiles for the dependent variables at the upstream computational boundary were obtained from a two-dimensional flat-plate calculation. This computation employed the identical numerical formulation and vertical grid distribution that was used for the roughness element simulation. Profiles were extracted at the streamwise location along the plate which most closely match the expected theoretical values of boundary-layer, momentum, and displacement thicknesses based upon the distance of the inflow boundary from the experimental virtual leading edge. Because not all three of these quantities could be matched at the same streamwise position, a least-squares fit was used to determine the optimal location. The inflow velocity profiles are compared with the Blasius solution in Fig. 3.

D. Boundary Conditions

Along the upstream boundary, all velocity components and the density were specified from the two-dimensional flat-plate solution. The pressure at this boundary was obtained by extrapolation from the interior domain. At the downstream outflow plane, the static pressure was fixed at the freestream value, and all other flow variables were extrapolated from within the domain. The downstream

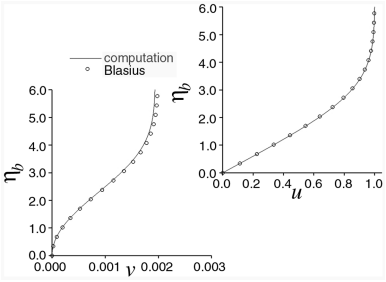

Fig. 3 Inflow velocity profiles.

computational mesh was intentionally severely stretched in the streamwise direction to prevent spurious reflections from the exit boundary. This technique transfers information to high streamwise spatial wave numbers, and then dissipates it by the low-pass filter [45].

On the upper domain boundary, the streamwise velocity component was specified as freestream u_∞ and the remaining variables were extrapolated from below. Excessive vertical grid stretching in this region, along with application of the numerical filter, again prevented spurious reflections. For all solid surfaces, consisting of the plate and side and top of the cylindrical element, the no-slip condition was enforced along with an isothermal wall and a zero normal pressure gradient. The specified isothermal temperature was the adiabatic wall value, and the pressure gradient condition was obtained with third-order spatial accuracy. Periodic conditions were applied along the spanwise boundaries, employing a five-grid point overlap in the z direction to maintain spatial accuracy.

E. Temporal Considerations

All computations were performed using a nondimensional time step (nondimensionalized using l and u_∞) of $\Delta t = 0.01$. The flowfield was initialized using the two-dimensional flat-plate result, and allowed to evolve sufficiently in time to remove transients and achieve an equilibrium state. Because of the low Mach number, this could require in excess of 2×10^5 time steps for each case. Once equilibrium was attained, the solution was processed for 2.8×10^5 time steps during which statistical information was collected. This duration represented approximately 10 characteristic time units based upon freestream conditions and the streamwise extent of the usable domain noted in Eq. (2).

IV. Results for $Re_k = 202$

A. Time-Mean Flowfield

A representation of the time-mean flowfield in the region close to the roughness element for $Re_k = 202$ appears in Fig. 4. Planar contours of the streamwise vorticity magnitude $|\omega_x|$ and streamlines comprising the horseshoe vortex system may be seen in the figure. The horseshoe system is composed of two corotating vortices: a primary vortex lying close to the cylinder, and a weaker secondary vortex upstream of the primary and nearer to the plate surface. It is

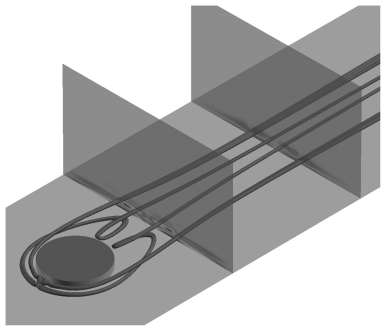

Fig. 4 Time-mean and instantaneous flowfield for $Re_k = 202$, showing planar contours of $|\omega_x|$ and streamlines of the horseshoe vortex system.

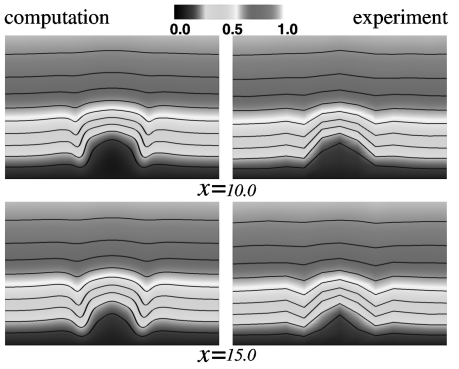

Fig. 5 Time-mean planar contours of the streamwise velocity component $\bar{u}$ for $Re_k = 202$.

noted that the most significant contributions to $|\omega_x|$ arise from the shear layer generated at the surface of the cylinder, rather than from the vortex system. This is because the horseshoe vortex system is weak. In this region of the domain, the amplitude of unsteady fluctuations is very small, so that the figure looks identical for the instantaneous flowfield.

Planar contours of the time-mean streamwise velocity $\bar{u}$, at a series of streamwise locations, are compared with experimental data in Fig. 5. Each frame of the figure represents the region defined by

$$0.0 \le \eta_b \le 4.0, \qquad -\lambda/2 \le z \le +\lambda/2 \tag{4}$$

Contour lines in the figure denote values of η_b where $\bar{u} = 0.1, 0.2, \ldots, 0.9$. The agreement between the computation and experiment is quite good at both streamwise locations. Additional comparisons at downstream stations appear in [25]. Similar contours from the computation alone are found in Fig. 6 at streamwise locations downstream of those at which measurements were taken. At the station furthest from the roughness element ($x = 200.0$), the flow has not returned to an undisturbed state.

A more detailed comparison of computed $\bar{u}$ profiles with those of the experiment is provided in Fig. 7. Profiles are shown at the centerline directly behind the roughness element ($z = 0.0$), and at the periodic boundary between elements ($z = \lambda/2$). Although it would appear the time-mean flowfield is approaching the Blasius state downstream ($x = 70.0$), that is not really the case. As evidenced by the contour levels in Figs. 5 and 6, the maximum deviation from a profile which is uniform in z occurs for $z \approx \pm 0.14\lambda$. Profiles at this location for downstream values of x are displayed in Fig. 8, where the variation from Blasius is obvious.

B. Instantaneous Flowfield

Planar contours of the fluctuating streamwise velocity u' from both the computation and the experiment are presented in Fig. 9. The region represented in frames of the figure corresponds to that of Eq. (4). The figure indicates that computed levels of u' are an order of magnitude lower than those of their experimental counterparts.

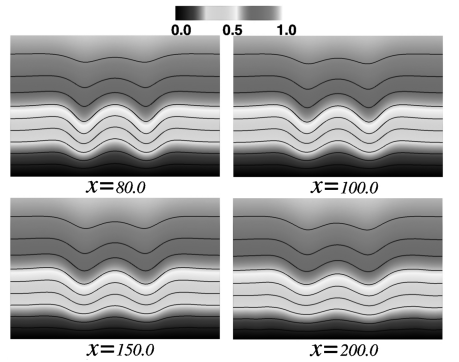

Fig. 6 Time-mean planar contours of the streamwise velocity component $\bar{u}$ for $Re_k = 202$.

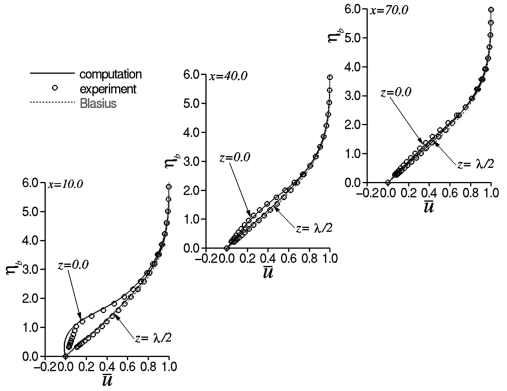

Fig. 7 Profiles of the time-mean streamwise velocity component $\bar{u}$ for $Re_k = 202$.

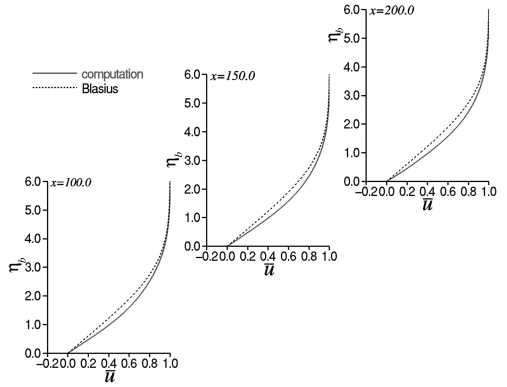

Fig. 8 Profiles of the time-mean streamwise velocity component $\bar{u}$ at $z = 0.14\lambda$ for $Re_k = 202$.

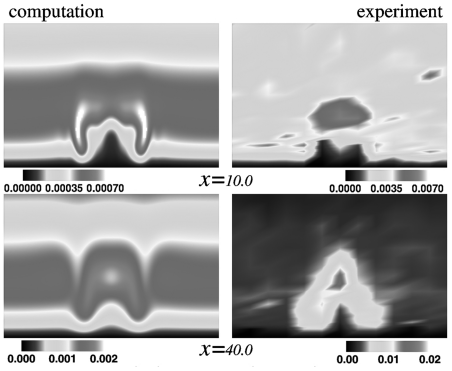

Fig. 9 Planar contours of the fluctuating streamwise velocity component u' for $Re_k = 202$.

Moreover, the numerically predicted values at $x = 10.0$ are less than the freestream levels of the experimental configuration used to collect the measured data [46]. Because the computation is devoid of any such freestream fluctuations, it cannot be expected that the direct numerical simulation should agree with the experiment, particularly near a transitional regime which is sensitive to such disturbances. For this reason, no further comparisons with the experimental measurements are made. Computed contours of u' at downstream stations appear in Fig. 10. For $x = 200.0$, u' begins to approach a homogeneous distribution in the spanwise direction.

Profiles of u' are found in Fig. 11. These were taken at the spanwise location of $z = 0.14\lambda$, where the time-mean velocity $\bar{u}$ had the maximum deviation from the Blasius profile. The figure illustrates a monotonic growth in the turbulence energy as the flow convects downstream. Other features of the instantaneous flowfield are displayed in Fig. 16 of [25].

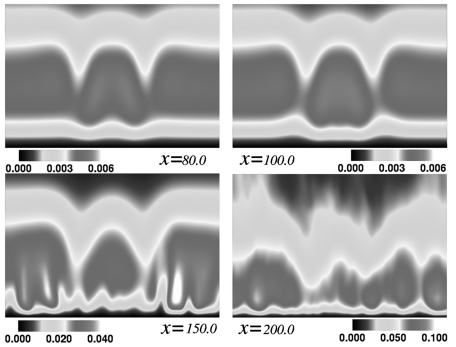

Fig. 10 Planar contours of the fluctuating streamwise velocity component u' for $Re_k = 202$.

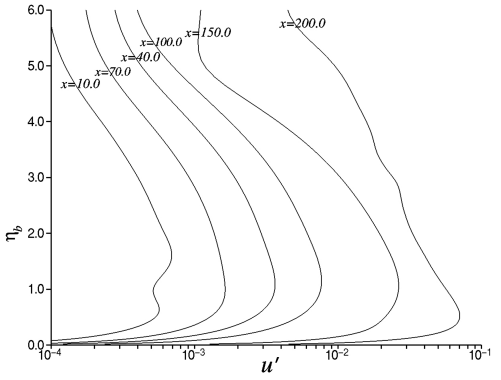

Fig. 11 Profiles of the fluctuating streamwise velocity component u' at $z = 0.14\lambda$ for $Re_k = 202$.

V. Results for $Re_k = 334$

The case of $Re_k = 334$ was specifically selected because it exhibited bypass transition to a fully turbulent state. It was believed that experimental data was available for comparison of time-mean $\bar{u}$ and fluctuating u' velocity components, as well as for turbulent energy frequency spectra. Unfortunately, due to a miscalibration of the roughness element height, no experimental data are available at this Reynolds number [47].

A. Time-Mean Flowfield

A representation of the time-mean flowfield, similar to that of Fig. 4 for $Re_k = 202$, is presented in Fig. 12. In this case, larger values of $|\omega_x|$ occur in a wider area than those of $Re_k = 202$ because the shear layer is stronger. The limiting surface streamline pattern on the plate surface is provided in Fig. 13. This figure illustrates the well-known diagram for a cylindrical object. All characteristic topological features of the surface behavior appear in the figure. A

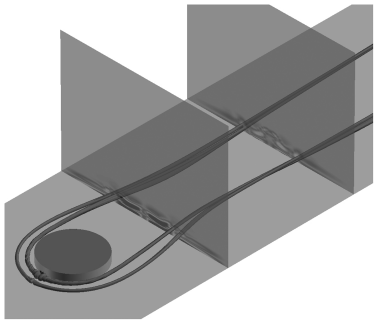

Fig. 12 Time-mean flowfield for $Re_k = 334$, showing planar contours of $|\omega_x|$ and streamlines of the horseshoe vortex system.

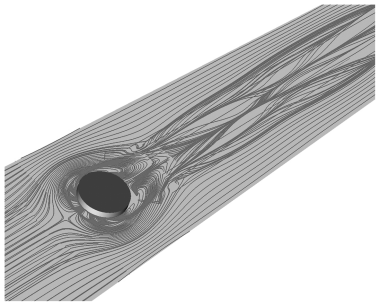

Fig. 13 Limiting surface streamline pattern on the plate surface ($y = 0.0$) of the time-mean flowfield for $Re_k = 334$.

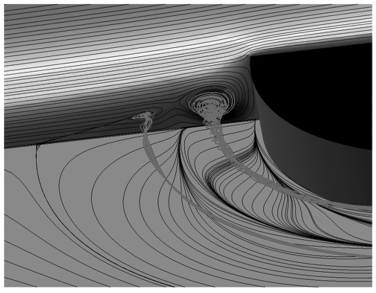

Fig. 14 Limiting surface streamline pattern on the plate surface ($y = 0.0$), planar contours of the streamwise velocity component $\bar{u}$ and limiting streamlines at the centerline ($z = 0.0$), and streamlines of the horseshoe vortices for the time-mean flowfield at $Re_k = 334$.

detailed description of these features may be found elsewhere [48], but is beyond the scope of the present discussion. Features of the time-mean flowfield near the cylinder leading edge are found in Fig. 14. At the centerline ($z = 0.0$), planar contours of $\bar{u}$ appear together with particle streamlines. Limiting streamlines are shown on the plate surface along with the streamlines defining the horseshoe system. Both the primary and secondary vortices are visible in the figure.

Figures 15 and 16 display planar contours of the time-mean streamwise velocity $\bar{u}$. These may be compared directly with those of Figs. 5 and 6 for $Re_k = 202$. Because the element is higher in this case, the shear layer forming at its surface is stronger, as is the horseshoe vortex system. Thus the velocity perturbation from Blasius flow is more substantial, as observed in the figures. At the downstream region ($x = 200.0$), the time-mean flow is becoming uniform in the z direction. Corresponding profiles of $\bar{u}$ are presented in Figs. 17 and 18. Also provided in the figures are results from a computation performed on the coarse computational mesh. At the centerline $z = 0.0$ for $x = 10.0$, a significant region of reverse flow is evident. The height of the element at this location is equivalent to $\eta_b = 1.43$. For the upstream stations ($x = 10.0$, 40.0), there is

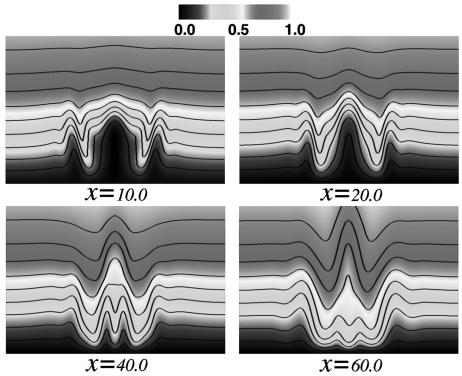

Fig. 15 Time-mean planar contours of the streamwise velocity component $\bar{u}$ for $Re_k = 334$.

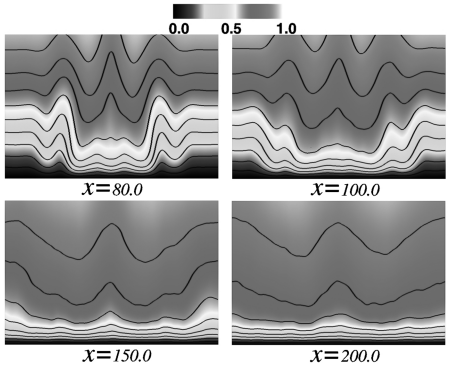

Fig. 16 Time-mean planar contours of the streamwise velocity component $\bar{u}$ for $Re_k = 334$.

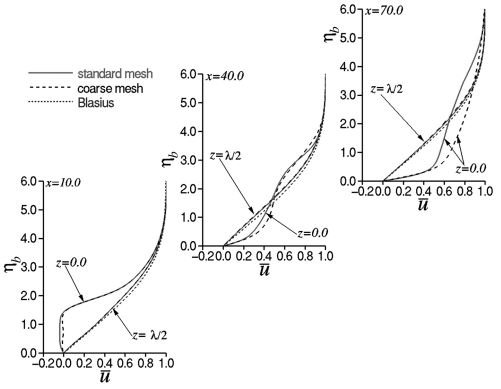

Fig. 17 Profiles of the time-mean streamwise velocity component $\bar{u}$ for $Re_k = 334$.

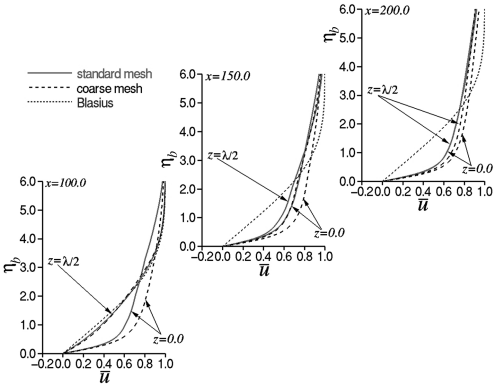

Fig. 18 Profiles of the time-mean streamwise velocity component $\bar{u}$ for $Re_k = 334$.

relatively good agreement between solutions on the two grids. As the flow begins to break down and transition to a turbulent state, the coarse mesh is incapable of supporting the fine-scale structures which arise. It should be remembered that the coarse mesh contains only one-eighth the total number of grid points as that of the standard grid. Nevertheless, the coarse-mesh solution was capable of predicting transition. As the flow evolves in the downstream direction, departure from the Blasius profile is apparent.

Profiles of the time-mean velocity $\bar{u}$ at $x = 200.0$ are indicated in Fig. 19. These profiles have been averaged in the spanwise direction, as the flow was becoming homogeneous in z (see Fig. 16). The lower left-hand frame of the figure gives the profile in law-of-the-wall coordinates, where a logarithmic layer is appearing. The upper right-hand frame compares $\bar{u}$ to the one-seventh power-law profile. The figure illustrates that although the flow may not yet have fully developed at this streamwise location, transition has in fact occurred.

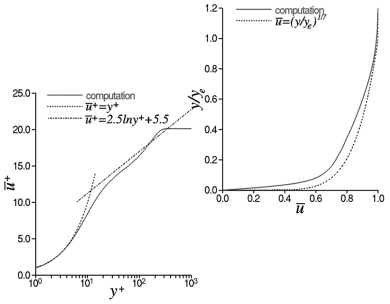

Fig. 19 Profiles of the spanwise-averaged time-mean streamwise velocity component $\bar{u}$ at $x = 200.0$ for $Re_k = 334$.

Based on the spanwise-averaged time-mean profile at $x = 200.0$, mesh spacings in wall units were found to have the values of

$$\Delta x^+ = 19.1 \qquad \Delta y_w^+ = 0.7 \qquad \Delta z^+ = 4.8 \tag{5}$$

which supports the description of a direct numerical simulation.

B. Instantaneous Flowfield

Planar contours of the fluctuating streamwise velocity u' appear in Figs. 20 and 21. Compared with similar contours for $Re_k = 202$ (Figs. 9 and 10), amplitudes of the fluctuations are generally an order of magnitude larger for streamwise stations where $x \leq 100.0$. Beyond $x = 100.0$, transition has occurred and spanwise homogeneity is approached at $x = 200.0$. Corresponding profiles of u' are found in Figs. 22 and 23 at the centerline $z = 0.0$ and at the periodic boundary $z = \lambda/2$. The growth in turbulence energy is much more explosive for this case than was apparent for $Re_k = 202$ (see Fig. 11). Profiles at $z = 0.0$ for $x = 10.0$ and $x = 40.0$ are characteristic of transitional flows, whereas those for $x \geq 100.0$ are representative of more fully developed turbulence. The coarse-mesh solution is seen to poorly capture the transitional region of development, but compares favorably with the standard-mesh result further downstream.

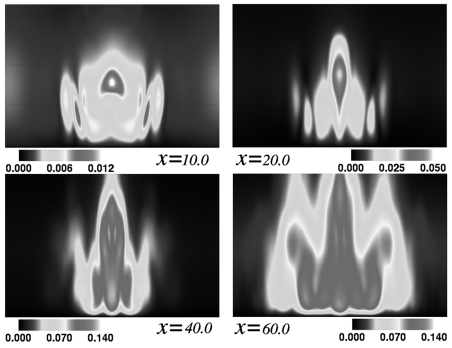

Fig. 20 Planar contours of the fluctuating streamwise velocity component u' for $Re_k = 334$.

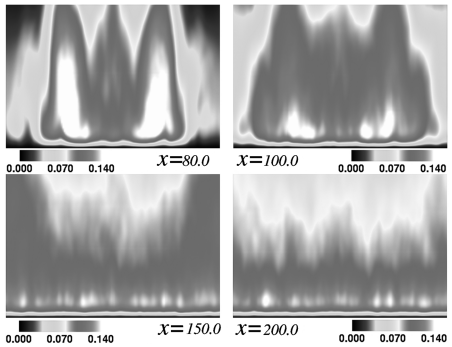

Fig. 21 Planar contours of the fluctuating streamwise velocity component u' for $Re_k = 334$.

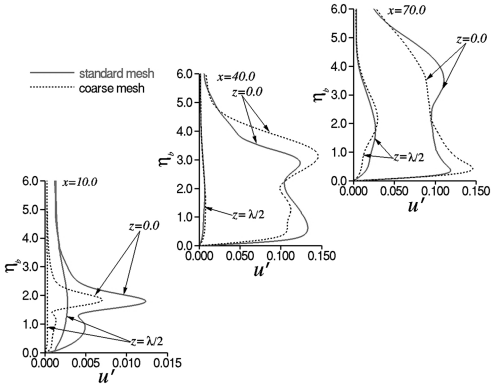

Fig. 22 Profiles of the fluctuating streamwise velocity component u' for $Re_k = 334$.

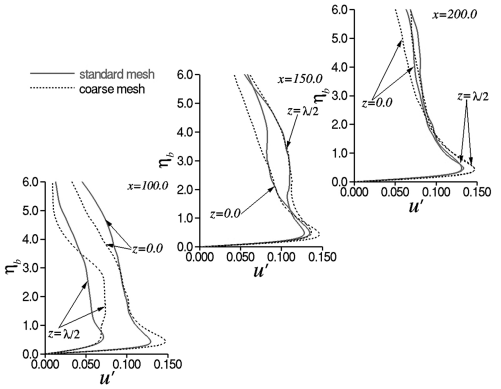

Fig. 23 Profiles of the fluctuating streamwise velocity component u' for $Re_k = 334$.

Planar contours of the instantaneous velocity components u, v, and w at the centerline $z = 0.0$ are displayed in Fig. 24. The vertical coordinate y in these contours has been stretched by a factor of 3.5 to enhance visibility of the features. Flow behind the roughness element is highly unsteady, unlike the situation for $Re_k = 202$ (see Fig. 16 of [25]). Small-scale structures are apparent for the vertical v and spanwise w components. The streamwise velocity u indicates an unstable shear layer arising from the top surface of the cylindrical element.

Instantaneous contours of the spanwise component of vorticity ω_z along the centerline ($z = 0.0$, side view) and on the plate surface ($y = 0.0$, top view) are presented in Fig. 25. In this figure, both the vertical y and spanwise z coordinates have been stretched, which is why the cylindrical element appears ovate in the top view. Near-wall structures, characteristic of turbulent flows, are visible at the downstream plate surface in the side view. The unstable shear layer is also evident immediately behind the roughness element. The top view showing the plate surface displays the footprint of low-speed

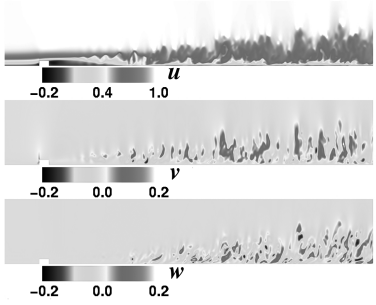

Fig. 24 Planar contours of the instantaneous streamwise u, vertical v, and spanwise w velocity components at the centerline $z = 0.0$ for $Re_k = 334$.

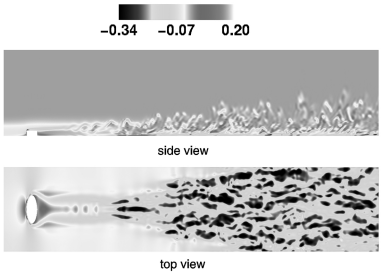

Fig. 25 Planar contours of the instantaneous spanwise component of vorticity ω_z at the centerline $z = 0.0$ and on the plate surface $y = 0.0$ for $Re_k = 334$.

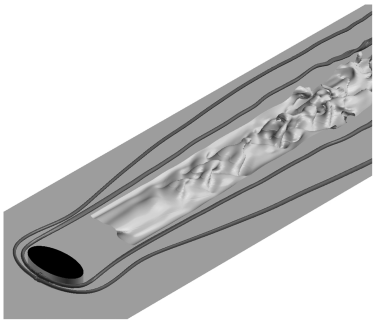

Fig. 26 Isosurface of the instantaneous total pressure and instantaneous streamlines for $Re_k = 334$.

streaks which are beginning to form in the near-wall region, and typify turbulent flows.

An instantaneous isosurface of total pressure and streamlines forming the horseshoe vortex system are shown in Fig. 26. The streamwise coordinate x has been scaled by 0.5 in the figure, and the isosurface value corresponds to the shear layer emanating from the surface of the roughness element. The unsteady shear layer, which was noted in Fig. 25, is characterized by hairpinlike vortical structures. This situation may be contrasted with that for $Re_k = 202$ (see Fig. 16 of [25]) where no shear-layer instability was observed. The hairpin vortices evolve as symmetric (in z) structures immediately downstream of the element. But as they grow in strength, they rapidly achieve a more random appearance. The growth eventually results in transition further downstream. Instability of the shear layer is exacerbated by its three-dimensionality, due to the finite spanwise extent of the roughness element. This process is identical to that which occurs for the flow past a hemispherical protuberance, which was extensively studied experimentally by Acarlar and Smith [49]. Breakdown of the unstable shear layer through the formation of hairpin vortices appears to be the fundamental route to transition for the case of $Re_k = 334$. The shear layer does not seem to be greatly affected by the presence of the horseshoe vortex system, although the interaction between the two could be important in the complex three-dimensional flowfield.

Found in Fig. 27 is an instantaneous isosurface and planar contours of $|\omega_x|$. The isosurface is meant to portray the three-dimensional flowfield and is colored by spatial variations in density. Changes in the density are extremely small as the flow is essentially incompressible, but the variations are used to highlight geometric variations in the isosurface. The planar contours illustrate formation of small-scale structures during the streamwise evolution of turbulence.

VI. Energy Growth and Spectra

Streamwise distributions of the planar integrated fluctuation energy E_i are seen in Fig. 28. Following the convention of Ergin and White [47], E_i is defined as

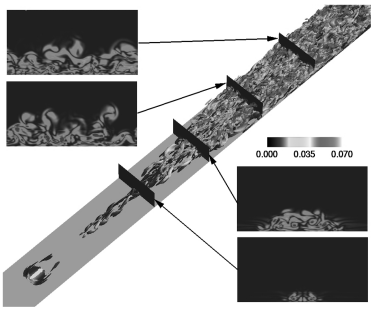

Fig. 27 Isosurface of instantaneous $|\omega_x|$ and planar contours of $|\omega_x|$ for $Re_k = 334$.

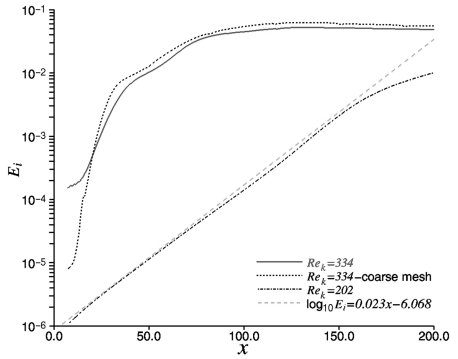

Fig. 28 Streamwise distributions of the planar integrated fluctuation energy for $Re_k = 202$ and $Re_k = 334$.

$$E_i = \frac{1}{\lambda}\int_{z=-\lambda/2}^{z=+\lambda/2}\int_{\eta_b=0}^{\eta_b=\infty}(u')^2\,\mathrm{d}\eta_b\,\mathrm{d}z \tag{6}$$

For $Re_k = 334$, the energy rapidly rises and achieves a plateau level at $x \approx 100.0$. The coarse-mesh result provides growth which is quite similar to that of the standard mesh. The $Re_k = 202$ case has an exponential streamwise growth, which has not yet attained a plateau level at the end of the computational domain. At $x = 200.0$, E_i for $Re_k = 202$ is still an order of magnitude lower than that of $Re_k = 334$. The $\log_{10}E_i$ appears to vary linearly with x for most of the streamwise extent. The form of energy growth observed here for $Re_k = 202$ was not seen in the investigation of Ergin and White [47]. In those experiments, the energy rose rather rapidly and then attained an equilibrium level at a fairly low amplitude, which was defined as transient growth. As pointed out earlier, however, freestream turbulence levels present in experimental facilities may lead to somewhat different physical situations.

Frequency spectra of $(u - \bar{u})^2$ at several streamwise locations are presented in Fig. 29. At $x = 50.0$ and $z = 0.0$, there appears to be a peak in the spectra at $f \approx 1000$ for $Re_k = 334$. The levels at $z = \lambda/2$ are substantially lower, and are lower still for $Re_k = 202$.

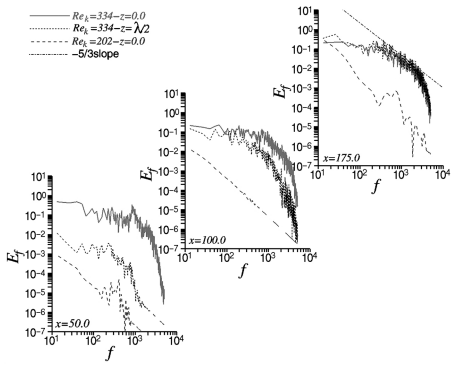

Fig. 29 Frequency spectra of $(u - \bar{u})^2$ at $\eta_b = 2.0$ for $Re_k = 202$ and $Re_k = 334$.

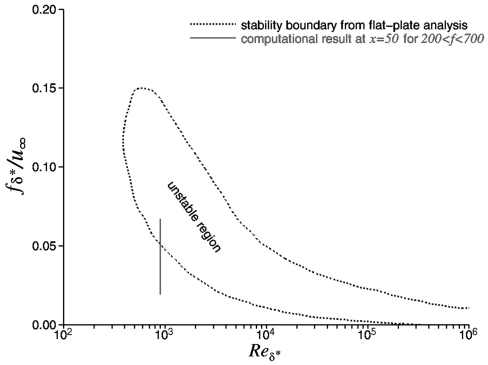

Fig. 30 Flat-plate stability diagram.

Amplitudes of E_f at $z = \lambda/2$ and $x < 150.0$ for $Re_k = 202$ are negligible, and have not been included in the figure. We make special mention of the fact that amplification in the spectra of $Re_k = 202$ at $x = 50.0$ occurs in the range $200 \leq f \leq 700$. At $x = 100.0$, the spectra for $Re_k = 334$ at $z = 0.0$ and $z = \lambda/2$ begin to coalesce and exhibit only broadband contributions, representative of turbulence. This behavior continues so that when $x = 175.0$, the spectra at $z = 0.0$ is indistinguishable from that at $z = \lambda/2$. Also at this location, the emergence of an inertial range ($-5/3$ slope) is evident.

The situation for $Re_k = 202$ is quite interesting. At $x = 100.0$, peaks in the frequency spectra which were present at $x = 50.0$ do not appear. Further downstream at $x = 175.0$, however, a peak in the energy level is observed, which is an order of magnitude higher than that at $x = 50.0$. This behavior might be explained by linear stability theory for the Blasius boundary layer. At $x = 50.0$, the displacement thickness-based Reynolds number Re_{δ^*} is approximately equal to 901. This is beyond the critical value of 420 for which an instability could possibly occur [50]. The frequency range of peaks in the spectra at $x = 50.0$ lie within the unstable region, as indicated by the stability diagram displayed in Fig. 30. Although the flow about the roughness element is inherently three-dimensional, and thus represents a more complex situation than can be addressed by two-dimensional stability theory, the limiting analysis could provide an explanation for the observed result.

Character of the spectra for $Re_k = 202$ at $x = 100.0$ is perhaps misleading. The integrated energy E_i is monotonically increasing with downstream distance, as was noted in Fig. 28. It could be expected that peaks in the frequency spectra would exist at other spanwise locations. As this behavior was not anticipated, however, spectral information at additional z locations was not recorded.

Turbulence energy spanwise wave number spectra for $Re_k = 334$ at two streamwise locations are shown in Fig. 31. These spectra have been temporally averaged. The figure indicates that resolution in the spanwise direction was adequate to capture fine-scale structures

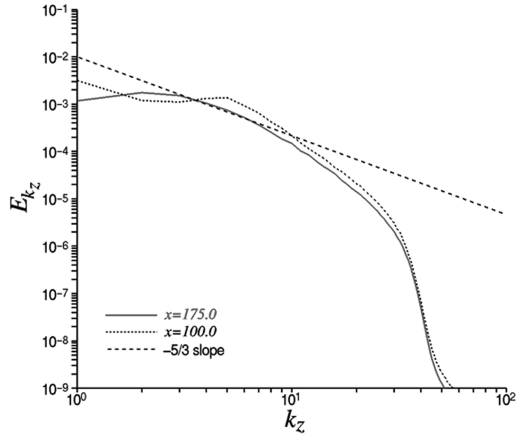

Fig. 31 Temporally averaged wave number spectra of $(u - \bar{u})^2$ at $\eta_b = 2.0$ for $Re_k = 334$.

arising during transition. It is also seen that an inertial range is evolving in the spectra.

VII. Summary and Conclusions

Direct numerical simulation was used to describe the flow past an array of distributed cylindrical roughness elements mounted on a flat plate. Computations were performed using a sixth-order-accurate numerical scheme and an overset grid methodology for describing the computational flowfield. A high-order interpolation procedure was employed to maintain accuracy at overlapping boundaries of distinct mesh systems that were used to define the roughness element.

Numerical flowfields were characterized by a system of weak corotating horseshoe vortices. For $Re_k = 202$, only low-amplitude fluctuations were observed in the streamwise domain near to the roughness element. Because of the absence of any large-scale unsteadiness, the time-mean and instantaneous flowfields were similar. Computed planar contours and profiles of the time-mean streamwise velocity component compared very well with experimentally measured data. The integrated turbulence energy was found to display exponential growth in the streamwise direction, and appeared to be approaching transition at the downstream extent of the computational domain. This behavior was not observed experimentally. Energy growth, however, was predicted by two-dimensional linear stability theory, and the computed result might indicate an alternate route to transition than that seen in some experiments.

Rather explosive bypass transition was displayed by the solution for $Re_k = 334$. Most of the dominant details of this process were also captured on a coarse-mesh simulation, thereby establishing confidence in the computed results. Transition was initiated downstream of the roughness element, by the breakdown of an unstable shear layer which formed about the element surface. Because of the finite lateral extent of the element, a spanwise instability in the shear layer gave rise to hairpin vortices which rapidly evolved to a chaotic situation. This course of events did not appear to be greatly influenced by the horseshoe vortex system, which seemed to play only a passive role in its development. At the downstream extent of the computational domain, the flow was approaching a fully turbulent state.

This investigation indicates that direct numerical simulation can help contribute to the understanding of flows past roughness elements and serve as a compliment to experimental measurements. Future efforts might focus on roughness-based Reynolds numbers lower than those considered here and attempt to determine the impact of low-amplitude incoming fluctuations upon the evolving behavior.

Acknowledgments

The work presented here was sponsored by the U.S. Air Force Office of Scientific Research and was monitored by R. W. Jefferies. Computational resources were supported in part by a grant of supercomputer time from the U.S. Department of Defense Major Shared Resource Centers at Stennis Space Center, Mississippi and Wright–Patterson Air Force Base, Ohio. The authors are indebted to E. B. White for providing results of his experiments to them, for his assistance in disseminating the data, and for a number of useful conversations. We also wish to acknowledge J. Poggie for several helpful discussions.

References

[1] White, E. B., Shelley, M. A., and Gurun, A. M., "Interactions of Tollmien–Schlichting Waves and Stationary Transient Disturbances," AIAA Paper 2004-2540, June–July 2004.

[2] White, E. B., "Transient Growth of Stationary Disturbances in a Flat Plate Boundary Layer," *Physics of Fluids*, Vol. 14, No. 12, Dec. 2002, pp. 4429–4439.

[3] Kendall, J., "Laminar Boundary Layer Velocity Distortion by Surface Roughness: Effect upon Stability," AIAA Paper 81-0195, Jan. 1981.

[4] Reshotko, E., and Leventhal, L., "Preliminary Experimental Study of Disturbances in a Laminar Boundary Layer Due to Distributed

Roughness," AIAA Paper 81-1224, June 1981.
[5] Breuer, K. S., and Haritonidis, J. H., "Evolution of a Localized Disturbance in a Laminar Boundary Layer, Part 1: Weak Disturbances," *Journal of Fluid Mechanics*, Vol. 220, Nov. 1990, pp. 569–594.
[6] Klebano, P. S., "Effect of Free-Stream Turbulence on a Laminar Boundary Layer," *Bulletin of the American Physical Society*, Vol. 16, No. 11, Nov. 1971, p. 1323.
[7] Kendall, J. M., "Experimental Study of Disturbances Produced in a Pre-Transitional Laminar Boundary Layer by Weak Freestream Turbulence," AIAA Paper 85-1695, July 1985.
[8] Westin, K. J. A., Boiko, A. V., Klingman, B. G. B., Kozlov, V. V., and Alfredsson, P. H., "Experiments in a Boundary Layer Subjected to Free Stream Turbulence, Part 1: Boundary Layer Structure and Receptivity," *Journal of Fluid Mechanics*, Vol. 281, Dec. 1994, pp. 193–218.
[9] Matsubara, M., and Alfredsson, P. H., "Disturbance Growth in Boundary Layers Subjected to Free-Stream Turbulence," *Journal of Fluid Mechanics*, Vol. 430, March 2001, pp. 149–168.
[10] White, E. B., and Reshotko, E., "Roughness-Induced Transient Growth in a Flat Plate Boundary Layer," AIAA Paper 2002-0138, Jan. 2002.
[11] White, E. B., and Ergin, F. G., "Receptivity and Transient Growth of Roughness-Induced Disturbances," AIAA Paper 2003-4243, June 2003.
[12] Ergin, F. G., and White, E. B., "Multicomponent and Unsteady Velocity Measurements of Transient Disturbances," AIAA Paper 2005-0527, Jan. 2005.
[13] Gurun, A. M., and White, E. B., "Tollmien–Schlichting Wave Suppression and Transition Delay Using Stationary Transient Disturbances," AIAA Paper 2005-5313, June 2005.
[14] Joslin, R. D., and Grosch, C. E., "Growth Characteristics Downstream of a Shallow Bump: Computation and Experiment," *Physics of Fluids*, Vol. 7, No. 12, Dec. 1995, pp. 3042–3047.
[15] Gaster, M., Grosch, C. E., and Jackson, T. L., "Velocity Field Created by a Shallow Bump in a Boundary Layer," *Physics of Fluids*, Vol. 6, No. 9, Sept. 1994, pp. 3079–3085.
[16] Fischer, P., and Choudhari, M., "Numerical Simulation of Roughness-Induced Transient Growth in a Laminar Boundary Layer," AIAA Paper 2004-2539, June–July 2004.
[17] Choudhari, M., and Fischer, P., "Roughness-Induced Transient Growth," AIAA Paper 2005-4765, June 2005.
[18] Beam, R., and Warming, R., "Implicit Factored Scheme for the Compressible Navier–Stokes Equations," *AIAA Journal*, Vol. 16, No. 4, April 1978, pp. 393–402.
[19] Gordnier, R. E., and Visbal, M. R., "Numerical Simulation of Delta-Wing Roll," AIAA Paper 93-0554, Jan. 1993.
[20] Jameson, A., Schmidt, W., and Turkel, E., "Numerical Solutions of the Euler Equations by Finite Volume Methods Using Runge-Kutta Time Stepping Schemes," AIAA Paper 81-1259, June 1981.
[21] Pulliam, T. H., and Chaussee, D. S., "Diagonal Form of an Implicit Approximate-Factorization Algorithm," *Journal of Computational Physics*, Vol. 39, No. 2, Feb. 1981, pp. 347–363.
[22] Lele, S. A., "Compact Finite Difference Schemes with Spectral-Like Resolution," *Journal of Computational Physics*, Vol. 103, No. 1, Nov. 1992, pp. 16–42.
[23] Visbal, M. R., and Gaitonde, D. V., "High-Order-Accurate Methods for Complex Unsteady Subsonic Flows," *AIAA Journal*, Vol. 37, No. 10, Oct. 1999, pp. 1231–1239.
[24] Gaitonde, D., Shang, J. S., and Young, J. L., "Practical Aspects of High-Order Accurate Finite Volume Schemes for Electromagnetics," AIAA Paper 97-0363, Jan. 1997.
[25] Rizzetta, D. P., and Visbal, M. R., "Direct Numerical Simulation of Flow Past an Array of Distributed Roughness Elements," AIAA Paper 2006-3527, June 2006.
[26] Gaitonde, D., and Visbal, M. R., "High-Order Schemes for Navier–Stokes Equations: Algorithm and Implementation into FDL3DI," U.S. Air Force Research Lab., TR AFRL-VA-WP-TR-1998-3060, Wright–Patterson AFB, OH, Aug. 1998.
[27] Gordnier, R. E., and Visbal, M. R., "Numerical Simulation of Delta-Wing Roll," *Aerospace Science and Technology*, Vol. 2, No. 6, Sept. 1998, pp. 347–357.
[28] Gordnier, R. E., "Computation of Delta-Wing Roll Maneuvers," *Journal of Aircraft*, Vol. 32, No. 3, May 1995, pp. 486–492.
[29] Visbal, M. R., "Computational Study of Vortex Breakdown on a Pitching Delta Wing," AIAA Paper 93-2974, July 1993.
[30] Visbal, M., Gaitonde, D., and Gogineni, S., "Direct Numerical Simulation of a Forced Transitional Plane Wall Jet," AIAA Paper 98-2643, June 1998.
[31] Rizzetta, D. P., Visbal, M. R., and Stanek, M. J., "Numerical Investigation of Synthetic-Jet Flowfields," *AIAA Journal*, Vol. 37, No. 8, Aug. 1999, pp. 919–927.
[32] Rizzetta, D. P., and Visbal, M. R., "Numerical Investigation of Transitional Flow Through a Low-Pressure Turbine Cascade," AIAA Paper 2003-3587, June 2003.
[33] Rizzetta, D. P., Visbal, M. R., and Blaisdell, G. A., "Time-Implicit High-Order Compact Differencing and Filtering Scheme for Large-Eddy Simulation," *International Journal for Numerical Methods in Fluids*, Vol. 42, No. 6, June 2003, pp. 665–693.
[34] Rizzetta, D. P., and Visbal, M. R., "Numerical Study of Active Flow Control for a Transitional Highly Loaded Low-Pressure Turbine," AIAA Paper 2005-5020, June 2005.
[35] Rizzetta, D. P., and Visbal, M. R., "Numerical Simulation of Separation Control for Transitional Highly Loaded Low-Pressure Turbines," *AIAA Journal*, Vol. 43, No. 9, Sept. 2005, pp. 1958–1967.
[36] Rizzetta, D. P., and Visbal, M. R., "Application of Large-Eddy Simulation to Supersonic Compression Ramps," *AIAA Journal*, Vol. 40, No. 8, Aug. 2002, pp. 1574–1581.
[37] Rizzetta, D. P., Visbal, M. R., and Gaitonde, D. V., "Large-Eddy Simulation of Supersonic Compression-Ramp Flow by a High-Order Method," *AIAA Journal*, Vol. 39, No. 12, Dec. 2001, pp. 2283–2292.
[38] Rizzetta, D. P., and Visbal, M. R., "Large-Eddy Simulation of Supersonic Cavity Flowfields Including Flow Control," *AIAA Journal*, Vol. 41, No. 8, Aug. 2003, pp. 1452–1462.
[39] Tani, I., "Boundary-Layer Transition," *Annual Review of Fluid Mechanics*, edited by W. R. Sears, Annual Reviews, Palo Alto, CA, 1969, pp. 169–196.
[40] von Doenhoff, A. E., and Braslow, A. L., "Effect of Distributed Surface Roughness on Laminar Flow," *Boundary Layer and Flow Control, Its Principles and Application*, edited by G. V. Lachman, Vol. 2, Pergamon, New York, 1961, pp. 657–681.
[41] Sherer, S. E., "Further Analysis of High-Order Overset Grid Method with Applications," AIAA Paper 2003-3839, Jun. 2003.
[42] Sherer, S. E., and Scott, J. N., "High-Order Compact Finite Difference Methods on General Overset Grids," *Journal of Computational Physics*, Vol. 210, No. 2, Dec. 2005, pp. 459–496.
[43] Suhs, N. E., Rogers, S. E., and Dietz, W. E., "PEGASUS 5: An Automated Preprocessor for Overset-Grid Computational Fluid Dynamics," *AIAA Journal*, Vol. 41, No. 6, June 2003, pp. 1037–1045.
[44] Message Passing Interface Forum, "MPI: A Message-Passing Interface Standard," Computer Science Dept. TR CS-94-230, Univ. of Tennessee, Knoxville, TN, April 1994.
[45] Visbal, M. R., and Gaitonde, D. V., "Very High-Order Spatially Implicit Schemes for Computational Acoustics on Curvilinear Meshes," *Journal of Computational Acoustics*, Vol. 9, No. 4, Dec. 2001, pp. 1259–1286.
[46] Ergin, F. G., "Roughness Induced Transition," Ph.D. Thesis, Case Western Reserve Univ., Cleveland, OH, 2005.
[47] Ergin, F. G., and White, E. B., "Unsteady and Transitional Flows Behind Roughness Elements," *AIAA Journal*, Vol. 44, No. 11, Nov. 2006, pp. 2504–2514.
[48] Visbal, M. R., "Structure of Laminar Juncture Flows," *AIAA Journal*, Vol. 29, No. 8, Aug. 1991, pp. 1273–1282.
[49] Acarlar, M. S., and Smith, C. R., "Study of Hairpin Vortices in a Laminar Boundary Layer, Part 1: Hairpin Vortices Generated by a Hemisphere Protuberance," *Journal of Fluid Mechanics*, Vol. 175, Feb. 1987, pp. 1–41.
[50] Schlichting, H., *Boundary-Layer Theory*, 6th ed., McGraw–Hill, New York, 1968.

Z. Wang
Associate Editor